

# Monolithic Chalcogenide Optical Nanocomposites Enable Infrared System Innovation: Gradient Refractive Index Optics

Myungkoo Kang, Laura Sisken, Charmayne Lonergan, Andrew Buff, Anupama Yadav, Claudia Goncalves, Cesar Blanco, Peter Wachtel, J. David Musgraves, Alexej V. Pogrebnyakov, Erwan Baleine, Clara Rivero-Baleine, Theresa S. Mayer, Carlo G. Pantano, and Kathleen A. Richardson\*

The size and weight of conventional imaging systems is defined by costly non-planar lenses and the complex lens assemblies required to minimize optical aberrations. The ability to engineer gradient refractive index (GRIN) optics has the potential to overcome constraints of traditional homogeneous lenses by reducing the number of components in optical systems. Here, an innovative strategy to realize this goal based on monolithic GRIN media created in Ge-As-Se-Pb chalcogenide infrared nanocomposites is presented. A gradient heat treatment to spatially modulate the volume fraction of high refractive index Pb-rich nanocrystals within a glass matrix is utilized, providing a GRIN profile while maintaining an optical transparency. A first-ever correlation of material chemistry and microstructure, processing protocol, and optical property modification resulting in a prototype GRIN structure is presented. The integrated approach and mechanistic understanding illustrated by this versatile modification paradigm provides a platform for new optical functionalities in next-generation imaging applications.

## 1. Introduction

Over the past several decades, chalcogenide glasses have seen expanded use in a wide range of bulk and planar optical components such as lenses<sup>[1–8]</sup> and waveguides.<sup>[9–11]</sup> This growth has been enabled by their broad transparency in the infrared (IR) region,<sup>[12–16]</sup> and more specifically, their tailorable refractive indices and physical properties made possible by their diverse chemistry<sup>[12]</sup> as well as their demonstrated compatibility with well-established bulk and planar film manufacturing processes.<sup>[17]</sup> To control and manipulate light propagation in an optical system, individual bulk optical components are typically fabricated into non-planar geometries and combined into multi-element lens stacks comprising multiple materials with differing optical properties.<sup>[1–8]</sup> Such legacy optical design and fabrication strategies often require

complex multi-step manufacturing processes which are costly, limit system design flexibility, and frequently lead to an increase in the size and weight of the resulting imaging system.<sup>[1–8,18]</sup> This challenge is especially impactful in bulk IR systems where high-density crystalline materials are commonly used, as these optical materials possess monochromatic/chromatic aberrations and limitations in performance at elevated temperatures.<sup>[19,20]</sup> Reducing size, weight, and extending performance (SWaP) of optical systems through the creation of IR nanocomposite materials possessing spatially tailorable gradient refractive index (GRIN) profiles provides a viable solution to this challenge.<sup>[19]</sup> The GRIN concept has been inspired by a wide range of phenomena observed in nature. For example, spatially varying refractive index profiles in human eyes enable imaging with good resolution and low aberration at both short and long distances.<sup>[21]</sup> The lessons learned from nature can now be used to control the steering of light in curved trajectories through, for example, a flat lens.<sup>[22–25]</sup> The opportunities GRIN flat lenses offer increase the design space and requisite volume needed for optical elements, enabling reduced size, weight, element count, and cost, thereby extending the trade space for optical performance parameters.<sup>[19,24–27]</sup> A material manufacturing paradigm


Dr. M. Kang, Dr. L. Sisken, Dr. C. Lonergan, A. Buff, Dr. A. Yadav, Dr. C. Goncalves, C. Blanco, P. Wachtel, Dr. J. D. Musgraves, Prof. K. A. Richardson  
CREOL

College of Optics and Photonics  
University of Central Florida  
Orlando, FL 32816, USA  
E-mail: kcr@creol.ucf.edu

Dr. A. V. Pogrebnyakov, Prof. T. S. Mayer  
Department of Electrical Engineering  
Pennsylvania State University  
University Park, PA 16802, USA

Dr. E. Baleine, Dr. C. Rivero-Baleine  
Missiles and Fire Control  
Lockheed Martin Corporation  
Orlando, FL 32819, USA

Prof. C. G. Pantano  
Department of Materials Science and Engineering  
Pennsylvania State University  
University Park, PA 16802, USA

 The ORCID identification number(s) for the author(s) of this article can be found under <https://doi.org/10.1002/adom.202000150>.

DOI: 10.1002/adom.202000150

that could exploit such novel functionality will modify the way optical systems are designed and one such strategy is discussed here.

Among the most critical challenges for designing a GRIN-containing optical component is finding a material and a refractive index modification process that satisfies multiple demanding requirements. These requirements include spatial control of the sign, magnitude, and spatial resolution of the refractive index change, transparency over a defined wavelength range, good thermal and mechanical stability, and compatibility with cost-effective manufacturing processes. Additionally, a candidate material must have low loss in the spectral window of use and possess the potential for a suitably large refractive index or dispersion modification, combined with the ability to spatially modulate that index modification. Arbitrary control of this profile, in either the lateral (a radial GRIN) and/or axial direction through the bulk optical component is an attractive “knob” designers would like to add to their toolbox, as such complex components in a “non-flat” geometry would not be viable using current manufacturing protocols. Most importantly, the resulting modification must have post-processed stability within defined operating conditions and be optically and physically compatible with other, non-GRIN materials. As reviewed in detail elsewhere,<sup>[28]</sup> GRIN profiles have been generated in oxide and non-oxide materials by a range of methods, including ion exchange<sup>[29]</sup> lamination of homogeneous dissimilar materials,<sup>[22,23,30,31]</sup> ion implantation,<sup>[32]</sup> and laser/electron beam exposure.<sup>[28,33–36]</sup> However, these methods typically require complex multi-step processes such as the fabrication of masks for incident laser/electron beam exposure to realize complex GRIN profiles,<sup>[34,36]</sup> are typically not amenable to large area modification,<sup>[29–32]</sup> generate optical losses associated with interfaces or implantation/irradiation-induced damage,<sup>[32]</sup> and result in modest (<0.01 refractive index unit, RIU) refractive index changes.

Controlled crystallization of glass with known crystallization behavior via a gradient thermal treatment addresses several of the issues. First, its simplicity and applicability for use with large components can substantially lower the overall component fabrication cost. Second, the crystallization of precisely sized, low absorption and scatter loss, high refractive index phases in the glass matrix can be spatially varied using gradient thermal treatments, yielding smoothly varying, quantitatively accurate GRIN profiles. Third, heat treatment (HT) does not create unnecessary microscopic damage to the medium, such as that typically seen with highly energetic (electron or ion-based) irradiation processes. Chalcogenide glasses have received increasing global interest over the past decade due to their suitability for use in bulk and planar IR optics.<sup>[1,12,14–16]</sup> With compositional tuning, their transparency can extend over the full IR spectral range from the visible and short-wave IR (SWIR) through the mid-wave IR (MWIR) to the long-wave IR (LWIR).<sup>[1,12,14–16,33,37–39]</sup> Recent activities have demonstrated how their crystallization behavior can be tailored through composition, morphology, and microstructural modification.<sup>[28,33–38,40–44]</sup> Recently, composites based upon Ge-As-Pb-Se chalcogenide glasses have been shown to yield high refractive index Pb-containing nanocrystalline phases in an amorphous matrix which can remain stable at elevated temperatures or under photo/electronically

excited states.<sup>[28,33–37,40–44]</sup> In the present approach, we exploit this simple yet effective process to transform multicomponent GeSe<sub>2</sub>-As<sub>2</sub>Se<sub>3</sub>-PbSe (GAP-Se) bulk glasses from an amorphous structure into an optical nanocomposite where the volume fraction of high refractive index Pb-rich nanocrystals is spatially varied in a low refractive index amorphous matrix, thereby realizing a GRIN structure with smoothly varying index and dispersion properties. Specifically, we explore the mechanism whereby thermal processing of GAP-Se glasses influences the nanocomposite's resulting microstructural and compositional evolution defining their post-processed transmissive and optical properties. We demonstrate how these factors can be used synergistically to produce optical components with GRIN profiles and quantified dispersion modification. This work illustrates a novel, first-ever integrated approach to the design–processing–structure–property–performance relationship employing gradient HT induced protocols to realize monolithic IR GRIN chalcogenide nanocomposites. These capabilities pave the way toward flat lenses and other optical components which can deliver complex optical function for traditional as well as next-generation imaging systems in a single (or fewer) component.

## 2. Results and Discussion

To effectively induce GRIN profiles with high spatial contrast across a chalcogenide glass–ceramic nanocomposite while maintaining its transparency over a broad IR spectral range, it is critical to understand the material's phase diagram which in turn allows selection of the starting glass composition and design of the post-processing parameters toward its functionalization. **Figure 1a** shows a 3D phase diagram of the GAP-Se system where a horizontal plane of its ternary (selenide compound) composition phase diagram at room temperature intersects with a vertical plane of a pseudo temperature–composition phase diagram.<sup>[33,37–41]</sup> First, the horizontal ternary composition phase diagram indicates the finite compositional space examined in this study. The compositions of varying PbSe content along the GeSe<sub>2</sub>-3As<sub>2</sub>Se<sub>3</sub> tie line demonstrates the alloying possible within a small subsection of compositions within GAP-Se's large glass-forming region. The methodology discussed herein can be extended beyond this series of compositions but is restricted in the present discussion to the series shown. The diagram is divided into amorphous and crystalline regions realized upon a rapid quenching of a conventionally melted compound from a temperature above its liquidus point to room temperature.<sup>[33,37–41]</sup> Since a post HT induced, spatially controlled formation of high-index crystalline phases with the maximum tunable extent of crystallinity within this matrix is the key to the realization of GRIN, the amorphous region of the phase diagram is required for the starting material. When Pb is systematically integrated into the glass network across this series' composition space, it does not disperse homogeneously.<sup>[38]</sup> This region of instability is further illustrated in the vertical phase diagram which depicts the morphological variation of the post-quenched glass as a function of PbSe content from 0 to 55 mol% along the tie line of a constant GeSe<sub>2</sub>:3As<sub>2</sub>Se<sub>3</sub> ratio.<sup>[33,37–39]</sup> Across this composition

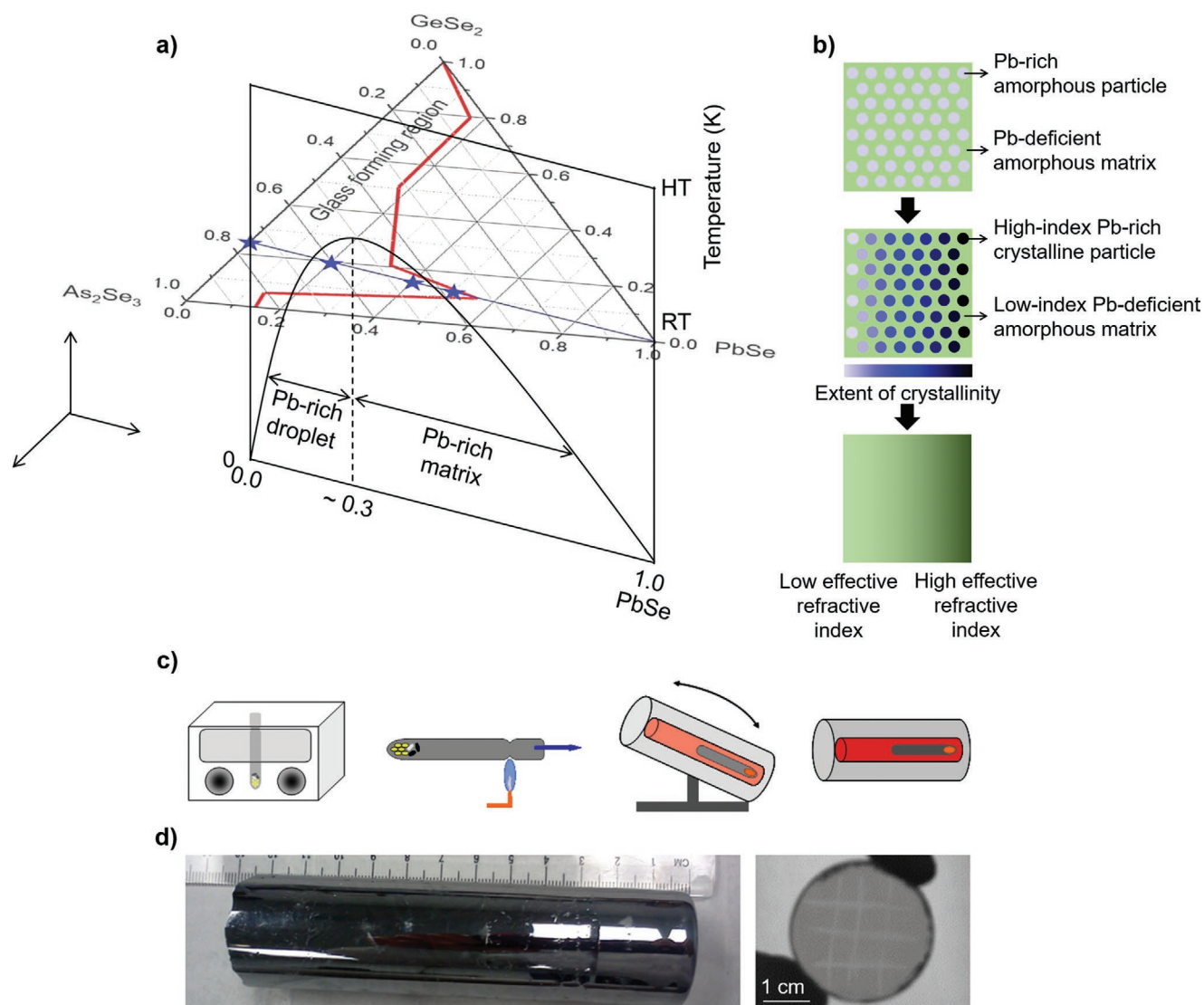


**Figure 1.** Design and fabrication of monolithic GRIN chalcogenide bulk glass-ceramics. a) 3D phase diagram of  $As_2Se_3$ - $GeSe_2$ - $PbSe$  system where the horizontal plane (triangle) is the glass' ternary compositional diagram at room temperature, and the vertical plane (parallelogram) represents a plot of temperature versus composition of  $(GeSe_2-3As_2Se_3)_{1-x}PbSe_x$  ( $0 \leq x \leq 1$ ) across the immiscibility region of the material. The red line on the horizontal ternary diagram corresponds to a compositional boundary between glass forming and spontaneously/randomly crystallized regions at room temperature. Representative compositions which possess a range of morphologies are chosen within and outside the immiscibility zone as shown by the stars. b) Schematic illustrating microstructural evolution upon quenching and following gradient thermal treatment with a resulting effective refractive index created within the glass ceramic composite. c) A fabrication process consisting of four steps: a quartz ampoule is used to contain batch source materials inside a nitrogen-filled glove box. The ampoule is then vacuum-pumped to evacuate air and sealed. The batch is melted using a rocking furnace and quenched to a glassy state. The glass specimen is subsequently annealed. d) A typical 400 g GAP-Se glass rod after rapid quench, anneal, and removal from the quartz ampoule (left) and a disk specimen (30 mm in diameter, 2 mm thick) cut from the same rod shown (right).

space, we have reported a zone of solid solution immiscibility with boundaries located between 5–10 and 40–45 mol%  $PbSe$  in conventionally melt-quenched chalcogenide glass batches up to 400 g in size. At and within these boundaries, glasses are solid solutions separating into Pb-rich and Pb-deficient amorphous phases. Specifically, for a region with  $PbSe$  content spanning  $\sim 5$ –25 mol%, a Pb-rich secondary phase emerges within a Pb-deficient matrix while the morphology gradually inverts becoming Pb-deficient secondary phases within a Pb-rich matrix as  $PbSe$  content increases beyond 30 mol% up to nominally 45 mol%. The phase-separated morphology observed

within the immiscibility zone dramatically influences the nucleation behavior of the post-HT crystalline phases that selectively occurs upon formation of the composite, as crystallite nucleation preferentially initiates in the Pb-rich containing phase. The size of the secondary Pb-rich and Pb-deficient amorphous phases typically range from  $\sim 100$  to  $\sim 250$  nm; as the reduced glass stability of the Pb-rich phase undergoes thermodynamic transformation to nuclei first (due to a lower activation energy barrier), the size of the resulting crystalline phase(s) created upon subsequent growth can remain sub-wavelength with precise selection of growth time and temperature, thereby

maintaining low loss and broadband transparency across the IR spectral region.<sup>[28,33–35,37,42–44]</sup>

The phase-separated parent glass can be transformed into a monolithic GRIN nanocomposite by a simple process for a representative 20 mol% PbSe material (Figure 1b). Here, the as-quenched glass comprising a Pb-rich amorphous secondary phase within a Pb-deficient amorphous matrix forms the starting morphology of the to-be crystallized composite. A gradient (furnace) HT is then applied to the glass where the extent of crystallization in the Pb-rich secondary phases is increased by a level proportional to the crystal growth rate at that temperature specific to the spatially varying temperature profile within the gradient furnace. This HT “develops” the microstructure thereby increasing the effective refractive index in this spatially varying region of the monolithic rod due to increasing extent of crystallization and resulting volume fraction of high-index crystalline phases along the direction of the thermal gradient (see Supporting Information). To experimentally demonstrate the process, the GRIN fabrication approach can be incorporated into a widely used, standard glass melt-quench process (Figure 1c).<sup>[33,37,38]</sup> First, a quartz tube is used as the melting crucible where elemental source materials are loaded into it within an atmosphere-controlled glove box. Once evacuated and sealed, the source material comprising the batch in the ampoule is melted and homogenized using a rocking furnace and rapidly quenched to the glassy state. The glass specimen is then annealed using a gradient HT to induce a GRIN profile. Figure 1d shows a lab-produced 400 g rod of a typical GAP-Se glass upon removal from the ampoule following this thermal protocol and a disk specimen cut and polished from the rod shown, when viewed with an IR camera.

Being able to identify and spatially map the microstructure and the composition of both as-quenched glasses and HT induced glass-ceramic resulting from the nucleation and growth of the high index nanocrystalline phase is the first key input to the GRIN fabrication process. **Figure 2a–h** shows transmission electron microscope (TEM) images and corresponding selected area electron diffraction (SAED) patterns collected from both as-quenched and heat-treated GAP-Se specimens with 0, 20, 40, and 50 mol% of PbSe. First, Figure 2a,b shows that as-quenched glasses with 0 and 50 mol% of PbSe, located outside the immiscibility zone,<sup>[33,37,38]</sup> are homogeneous and amorphous as indicated in their featureless dark field (DF) TEM images and diffuse rings in the corresponding SAED patterns. Figure 2c shows the same set of data where an increase in the content of PbSe to 20 mol% in the immiscibility zone involves the morphological evolution from a featureless matrix to secondary (amorphous) phases within an amorphous matrix as indicated by the bright, circular phases in a dark matrix. The contrast between the secondary phases and the matrix in the DF TEM image along with diffuse rings in the SAED pattern suggests that the atomic percentage of heavy constituents in the secondary phases is greater than that in the matrix while the entire nanocomposite remains amorphous. A HT of the GAP-Se glass with 20 mol% of PbSe selectively crystallizes the Pb-rich secondary phases as shown in Figure 2d,e where asymmetric shapes of the secondary phases appear in the DF TEM image. These images illustrate the coexistence

of crystalline spots and diffuse rings in the SAED pattern, and the crystalline fringes existing exclusively within the dark, secondary phases in the high-resolution bright field (BF) TEM image coherently indicate the emergence of Pb-containing nanocrystals. A further increase in the content of PbSe to 40 mol% and a subsequent HT of the composition in the immiscibility zone induces inverse microstructures of the pre- and post-annealed GAP-Se glass with 20 mol% of PbSe (i.e., Pb-deficient secondary phases within a Pb-rich matrix), as shown in Figure 2f–h.

Spatial distributions of constituents in the phase-separated GAP-Se glasses with 20 and 40 mol% of PbSe in the composition space of interest are quantified. Specifically, the X-ray energy dispersive spectroscopy (XEDS) maps of constituents collected from the GAP-Se glass with 20 mol% of PbSe indicate a strong, qualitative match between the distribution of Pb and that of the secondary phases in the DF TEM image (Figure 2i). Figure 2j shows the atomic percentages of these four constituents quantified along the line across several secondary phases and matrix regions from the DF TEM image in Figure 2i, where it is clear that the secondary phase and the matrix are Pb-rich and Pb-deficient, respectively. It can be seen that the spatial distributions of As and Ge are opposite to that of Pb while the distribution of Se remains relatively uniform across the region studied. Likewise, the EELS maps of constituents collected from the GAP-Se glass with 40 mol% of PbSe indicate that the spatial distribution of Pb strongly matches that of the matrix in the DF TEM image (Figure 2k). Here, the corresponding spatial atomic percentages of four constituents in Figure 2l indicate an inverse microstructure to that of the 20 mol% of PbSe glass where the secondary phase and the matrix are Pb-deficient and Pb-rich, respectively. The segregation of Pb at the sub-wavelength scale has a particular importance since Pb-containing crystalline phases such as PbSe and  $\text{Ge}_{0.1}\text{Pb}_{0.9}\text{Se}$ , which are formed dominantly within the Pb-rich regions upon HT, possess refractive indices far greater than those of other resulting crystalline phases, including  $\text{As}_2\text{Se}_3$  and Se as well as that of the surrounding amorphous counterpart, thereby increasing the effective refractive index of a resulting glass-ceramic nanocomposite.<sup>[33–37,42,44]</sup> Furthermore, while the spatial segregation of Pb is universally shown in GAP-Se glasses with a given mol% of PbSe in the immiscibility zone, the extent of the segregation varies with the average diameter of the secondary phases (see Figure S1, Supporting Information), indicating the metastable, non-equilibrium kinetic nature of the phase separation.<sup>[45]</sup>

Following analyses of morphology and composition of the starting glasses and resulting glass-ceramics, the identification of crystalline phases and their attributes (size, number density) formed upon HT is the next key factor toward prediction of the index modification within a specific parent glass composition and the ultimate GRIN profile achievable. **Figure 3a** shows Raman spectra collected from GAP-Se glasses with 20 mol% of PbSe annealed over a wide range of temperatures from 180 to 240 °C. Two prominent peaks are observed at wavenumbers of 205 and 246  $\text{cm}^{-1}$ . The peak located at 205  $\text{cm}^{-1}$  corresponds to  $\text{GeSe}_2$ .<sup>[33,34,46,47]</sup> The band centered at a wavenumber of 246  $\text{cm}^{-1}$  consists of two major peaks located at wavenumbers of 225 and 240  $\text{cm}^{-1}$ , both of which correspond to primary bands associated with As-Se vibrations seen in  $\text{As}_2\text{Se}_3$ ,



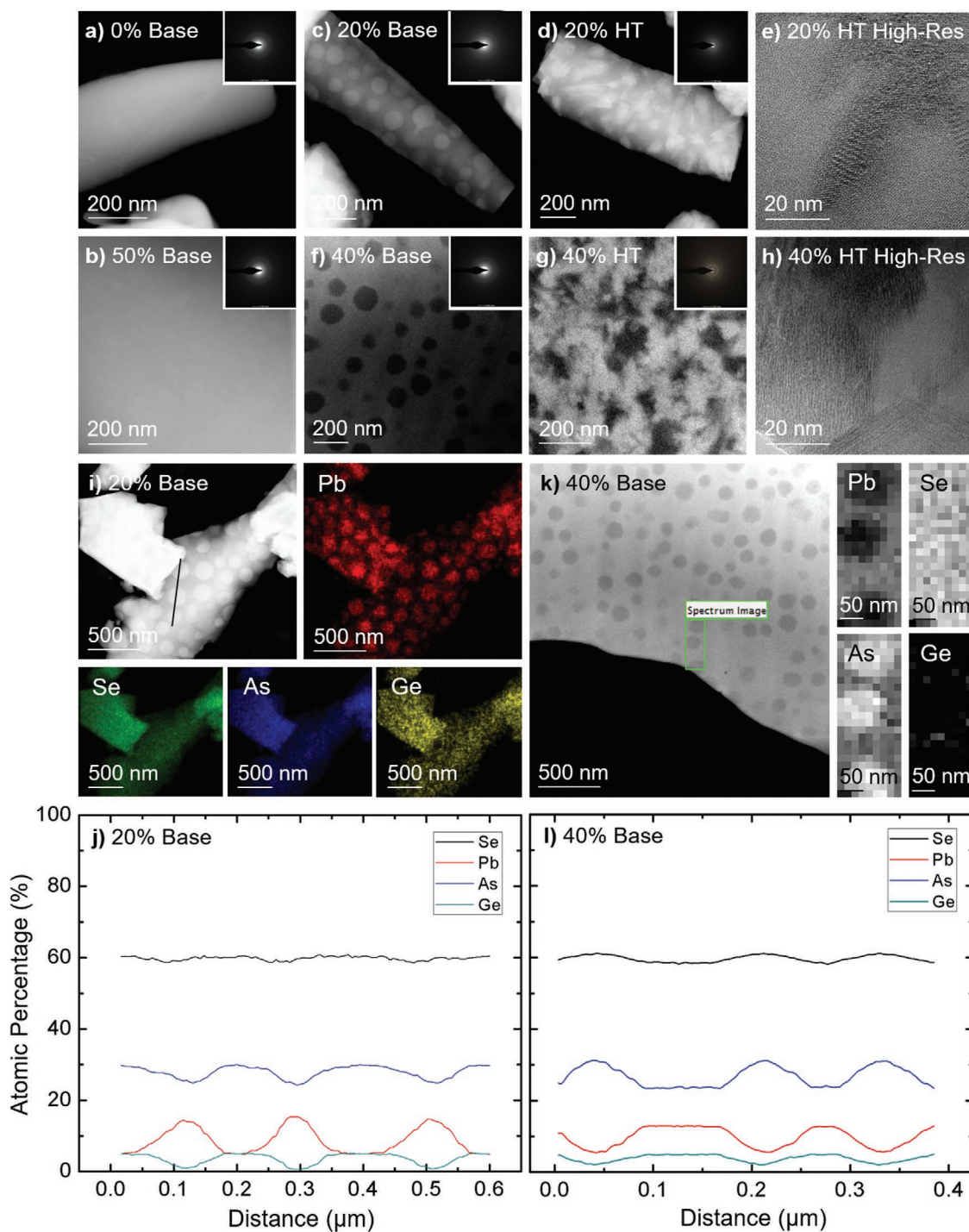


**Figure 2.** GAP-Se morphology and compositions. TEM images and SAED patterns from a) a base specimen with 0 mol% PbSe (DF), b) a base specimen with 50 mol% PbSe (DF), c) a base specimen with 20 mol% PbSe (DF), d) a heat-treated specimen with 20 mol% PbSe (DF), e) a heat-treated specimen with 20 mol% PbSe (BF, high-resolution), f) a base specimen with 40 mol% PbSe [DF], g) a heat-treated specimen with 40 mol% PbSe (DF), and h) a heat-treated specimen with 40 mol% PbSe (BF, high-resolution). The HT was conducted for 8 h at 230 °C. i) A DF TEM image from a base specimen with 20 mol% PbSe and XEDS images of Pb, Se, As, and Ge. j) Atomic percentages of the constituents along the line on the TEM image in (i). k) A DF TEM image from a base specimen with 40 mol% PbSe and EELS images of the constituents. l) Atomic percentages of the constituents along the line on the TEM image in (k).

with a shoulder located at a wavelength of  $250\text{ cm}^{-1}$  originating from a peak corresponding to Se.<sup>[33,34,46,47]</sup> As HT temperature surpasses 200 °C, the intensity of the peak at  $246\text{ cm}^{-1}$  substantially decreases while that of the peak at  $205\text{ cm}^{-1}$

remains within a similar intensity, as indicated by the dotted lines in Figure 3a. This suggests conversion of species from one bonding configuration to another during the thermal treatment. Figure 3b illustrates the ratio of the peak intensity at 205

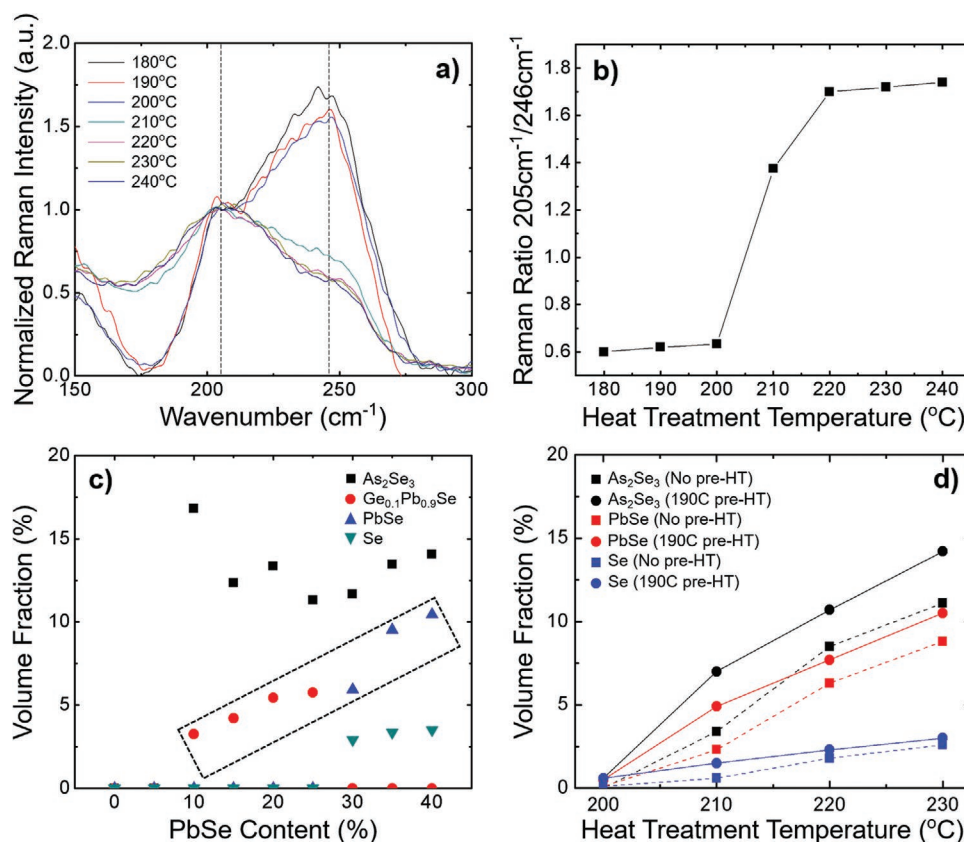


**Figure 3.** HT and crystallization in GAP-Se materials. a) Normalized Raman spectra of 20 mol% PbSe specimens heat treated for 30 min at various temperatures including 180, 190, 200, 210, 220, 230, and 240  $^{\circ}\text{C}$ . The two vertical dashed lines at the two key wavenumbers of 205 and 246  $\text{cm}^{-1}$  are guides to the eye. b) Corresponding ratios of Raman intensities at 205 and 246  $\text{cm}^{-1}$  (shown in (a)) as a function of HT temperature. c) Volume fraction of crystalline  $\text{As}_2\text{Se}_3$ ,  $\text{Ge}_{0.1}\text{Pb}_{0.9}\text{Se}$ ,  $\text{PbSe}$ , and  $\text{Se}$  observed in specimens with varying mol% of PbSe following HT. d) Crystalline phase volume fraction evolution for the crystalline phases observed in parent glass specimens (40 mol% PbSe) following various HT protocol.

to that at 246  $\text{cm}^{-1}$  as a function of HT temperature, where a transition in structure between 200 and 220  $^{\circ}\text{C}$  occurs. The clear transition shown in the ratio of  $\text{GeSe}_2$  to  $\text{As}_2\text{Se}_3$  bonds is likely due to the conversion of As–Se bonds in the starting amorphous configuration to  $\text{As}_2\text{Se}_3$  bonds in the resulting crystalline configuration.<sup>[46,47]</sup>

To identify the type and the quantity of crystalline phases formed upon HT of a wide range of composition spaces, GAP-Se glasses with compositions ranging from 0 to 40 mol% of PbSe were subjected to the same HT protocol at a temperature beyond the onset of crystallization. The volume fractions of crystalline phases extracted from X-ray diffraction patterns of the glass-ceramics<sup>[33,34,42]</sup> are then plotted as a function of the parent glass' PbSe content (Figure 3c). GAP-Se glass-ceramics with 0–25 mol% of PbSe exhibit two crystalline phases including  $\text{As}_2\text{Se}_3$  and  $\text{Ge}_{0.1}\text{Pb}_{0.9}\text{Se}$  while GAP-Se glass-ceramics with 30–40 mol% of PbSe exhibit three crystalline phases, including  $\text{As}_2\text{Se}_3$ ,  $\text{PbSe}$ , and  $\text{Se}$ . The dominance of  $\text{As}_2\text{Se}_3$  crystals is consistent with Raman data in Figure 3a,b. Most importantly, the volume fraction of the Pb-containing high-index phases including  $\text{Ge}_{0.1}\text{Pb}_{0.9}\text{Se}$  and  $\text{PbSe}$  monotonically increases with PbSe content, indicating that an increase in the effective refractive index of the nanocomposite upon HT will likely occur with high index species forming at the expense

of the parent glass species. To quantify how the volume fractions of different crystalline phases evolve with increasing HT temperature, fractions of  $\text{As}_2\text{Se}_3$ ,  $\text{PbSe}$ , and  $\text{Se}$  crystals in heat-treated GAP-Se glasses with 40 mol% of PbSe are plotted as a function of HT temperature ranging from 200 to 230  $^{\circ}\text{C}$  (Figure 3d). The volume fractions of all the crystalline phases monotonically increase with HT treatment temperature, and their respective ratios are maintained, indicating that the effective refractive index of a glass-ceramics is expected to likewise monotonically increase with HT temperature. While glass with and without pre-HT all exhibit an increase in volume fraction of crystals formed (and the desired Pb-containing high refractive index phase), the effect of a pre-HT step results in post-HT'd media with a much narrower nanocrystallite size distribution resulting in reduced optical scatter. This is attributed to the formation of nuclei at the pre-HT temperatures available for subsequent growth, as compared to random, spontaneous crystallization of a broad size range of crystals, realized with no nucleation HT step.

To ascertain how both the parent glass composition and the HT temperature protocol led to optical property evolution in the resulting GAP-Se glass-ceramics, effective refractive indices of GAP-Se glasses with 20 and 40 mol% of PbSe were evaluated. Here, specimens had undergone one- or multi-step HT

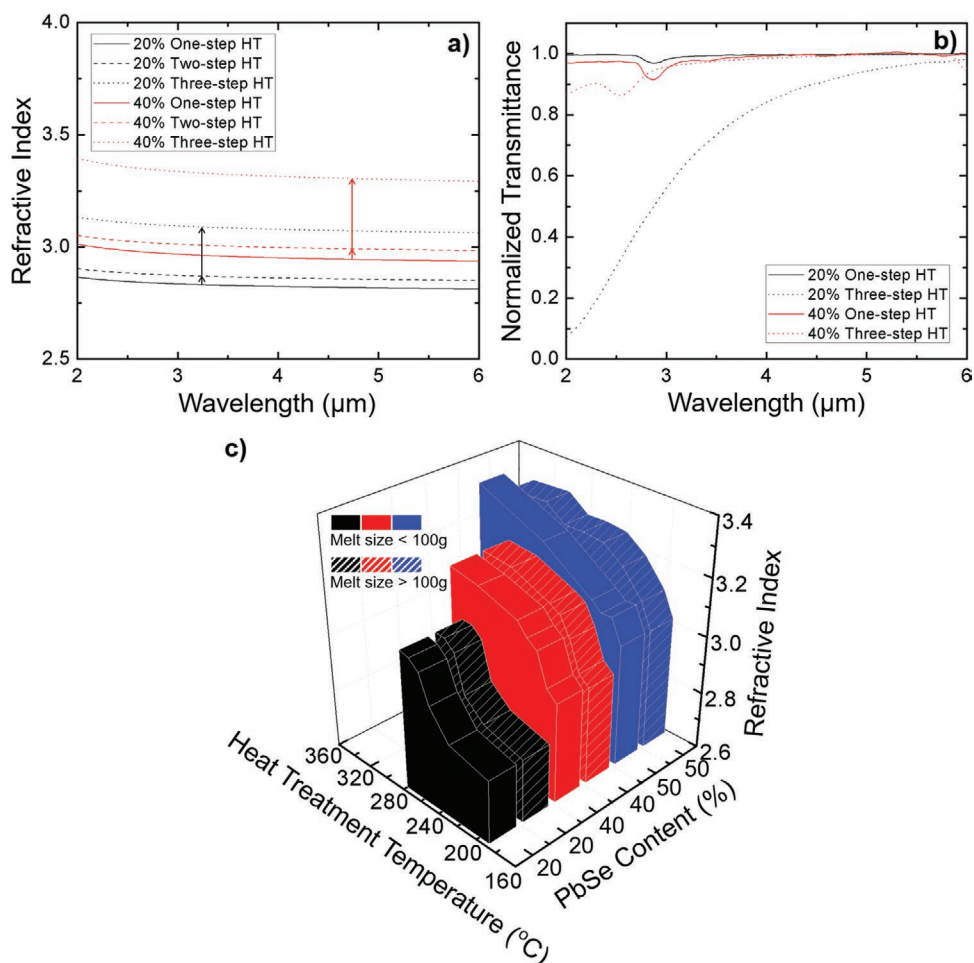


**Figure 4.** Engineering optical properties of GAP-Se glass-ceramics. a) MWIR index spectra of specimens with 20 mol% (black) and 40 mol% (red) PbSe following either one- or multi-step HT protocols at various temperatures (one-step: 16 h at 190 °C; two-step: 16 h at 190 °C + 2 h at 220 °C; and three-step: 16 h at 190 °C + 2 h at 220 °C + 2 h at 270 °C). The vertical arrows correspond to increases in refractive index of specimens with 20 and 40 mol% PbSe as a function of HT protocol. b) MWIR transmittance spectra (normalized at  $\lambda = 7 \mu\text{m}$ ) of specimens with 20 and 40 mol% PbSe following one- and three-step HT in (a). c) A 3D plot correlating three factors responsible for property change in GAP-Se material, including PbSe content, HT temperature, and refractive index, as measured at  $\lambda = 4.5 \mu\text{m}$  for specimens with 20, 40, and 50 mol% PbSe. Included for comparison are behavior seen in small melts (<100 g) as compared to large melts (>100 g).

at temperatures of 190, 220, and 270 °C and were measured in the MWIR region from 2 to 6  $\mu\text{m}$  using spectroscopic ellipsometry (Figure 4a). Under each HT protocol, the effective refractive index increases with PbSe-containing crystallite content, as indicated by the comparison of plots in same types (i.e., solid, dashed, and dotted), due to the increase in the volume fraction of Pb content which can be converted into high-index, Pb-containing crystalline phases upon HT, as discussed in Figure 3c. Within each composition, this effective refractive index increases with higher and longer HT, as indicated by the vertical arrows, due to the increase in volume fraction of high-index phases discussed in Figure 3d. The maximum net increase in the effective refractive index of  $\approx 0.37$  is achieved using the HT of the GAP-Se glasses with 40 mol% of PbSe at 220 °C. Figure 4b shows the corresponding MWIR transmittance spectra collected from the heat-treated GAP-Se glasses with 20 and 40 mol% of PbSe using a Fourier-transform IR spectrometer. For both 20 and 40 mol% of PbSe, the HT with

higher temperature and longer time induces a decrease in the transmittance (to a greater extent for 20 mol% of PbSe) due to the crystalline phase induced optical scattering.<sup>[33,34,42]</sup> This scattering manifests at the shortwave edge of the transmission scan leaving mid- and long-wave transmission largely unaffected. This observation confirms that the resulting glass-ceramic nanocomposites behave like transparent effective medium in the long-wave IR region. A wide range of compositions and HT temperatures were explored to construct a universal relationship with resulting refractive indices, as summarized by the 3D diagram (Figure 4c). From this figure, one observes that an increase in PbSe content and/or HT temperature leads to an increase in the effective refractive index of a GAP-Se glass. Also, it is important to note that the melt size as well as the thermal history of the melt and its impact on resulting starting glass morphology<sup>[44]</sup> has a negligible effect on the resulting refractive index change upon HT, indicating the repeatability and scalability of material response. Meanwhile, an upper limit



of the thermal process' scalability to be at a point where the time required for the component to reach a thermal equilibrium for a defined temperature gradient profile (as determined by the component's thermal conductivity and size) becomes prohibitive. Under such conditions, a significant fraction of time assigned for thermal treatments to independently control nucleation and growth kinetics are no longer attainable. This universal diagram provides information as to how a composition and a thermal treatment temperature could be combined and optimized to achieve a specific refractive index change, thereby creating a "look up table of processing variables" that results in fabrication requirements needed to create a target GRIN profile.

To utilize the mechanistic understanding of controlled nucleation and growth realized in the present sections toward the creation of a GRIN profile with quantified induced optical modification and function, a 50 mm long, as quenched and nucleated 20 mol% PbSe GAP-Se glass underwent HT (growth) within a gradient furnace. Here, the temperature extremes of the rod spanned temperatures of 225 °C near the furnace's "cold" end and 260 °C near its "hot" end. **Figure 5a** shows how the resulting glass-ceramic rod upon gradient HT was cut into slices for subsequent microstructural and optical characterizations. The two BF TEM images collected from slices 1 and 10, corresponding to temperatures in the gradient heat profile are 225.6–229.4 °C and 261.4–263.2 °C, respectively, show that the asymmetric nature of the bright, Pb-rich secondary phases in its dark matrix of slice 10 is much greater than that of slice 1. This microstructural difference confirms that the slice seeing higher HT (growth temperatures) possesses a higher volume fraction of Pb-rich crystalline phases. MWIR refractive index spectra collected from slices 3, 6, 8, and 10 are shown in **Figure 5b**, where the value of effective index monotonically increases as the extent of crystallization increases. **Figure 5c** shows spectral optical losses represented by the imaginary part of a complex refractive index<sup>[48]</sup> collected from the same slices. The optical losses for all slices remain within a similar range and decrease as wavelength increases, which is consistent with the recovery of transmittance spectra discussed in **Figure 4b**. As the fraction of crystal and glass in the glass ceramic changes as the extent of crystal formation (conversion) increases, one might expect this to impact the resulting optical composite's dispersive properties. The Abbe number is a crucial parameter quantifying the dispersion of a refractive index spectrum, and the MWIR Abbe number is formulated as follows:

$$\text{MWIR Abbe number} = V_{\text{MWIR}} = \frac{n_{\lambda=4\mu\text{m}} - 1}{n_{\lambda=3\mu\text{m}} - n_{\lambda=5\mu\text{m}}} \quad (1)$$

where  $n_{\lambda} = 3 \mu\text{m}$ ,  $n_{\lambda} = 4 \mu\text{m}$ ,  $n_{\lambda} = 5 \mu\text{m}$  correspond to effective refractive indices of a material at wavelengths of 3, 4, and 5  $\mu\text{m}$ , respectively.<sup>[23,33,36,39,42]</sup> The corresponding MWIR Abbe numbers extracted using the spectra in **Figure 5b** are plotted in **Figure 5d** where the indices and Abbe numbers spatially vary along the heat-treated GAP-Se rod. Such changes to the SWIR and LWIR dispersion also occur.<sup>[36,42]</sup> Notably, this specific HT protocol and the straightforward conversion of a parent glass with this composition induces a refractive index and MWIR

Abbe number gradients of  $\approx 0.2$  and  $\approx 35$ , respectively. Hence, the ability to create GRIN profiles within a non-curved, transparent medium enabled by such spatially varying conversion suggests that this technique will increase design flexibility for imaging applications such as flat lenses and other optical components. Furthermore, **Figure 5d** implies that the dispersive nature of GAP-Se ChG glasses and glass-ceramics can be systematically tuned using variable thermal treatment conditions.

To illustrate the dispersion engineering enabled by the glass ceramic formation process, **Figure 5e** shows a refractive index dispersion map for groups of optical and IR materials, including chalcogenides, III-V and IV semiconductors, II-VI semiconductors, fluorides, oxides, and alkali halides.<sup>[49]</sup> To correctly represent the curvature of index dispersion along two orthogonal directions in a 2D space, the map is constructed by Abbe number and partial refractive index which is defined by the following equation:<sup>[49]</sup>

$$\text{MWIR partial refractive index} = P_{\text{MWIR}} = \frac{n_{\lambda=3\mu\text{m}} - n_{\lambda=4\mu\text{m}}}{n_{\lambda=3\mu\text{m}} - n_{\lambda=5\mu\text{m}}} \quad (2)$$

The map clearly shows that each group of materials can be characterized by specific locations due to their intrinsically-similar electronic structures and resulting light-matter interactions within each group. However, most material systems shown in the map have a *single*  $V_{\text{MWIR}}-P_{\text{MWIR}}$  signature, indicating that the materials are bound to very narrow ranges of dispersion. Unlike these homogenous optical materials, the dispersive nature of the GAP-Se system shown herein can be simply tuned by converting it to a glass-ceramic optical composite. Here, variation in the extent of crystal phase formation is the key "knob" in altering the composite's effective index and dispersion. **Figure 5f** quantitatively depicts this "tunability" of dispersive properties for GAP-Se upon HT where the polygons correspond to the ranges of  $V_{\text{MWIR}}-P_{\text{MWIR}}$  values enabled by current HT protocols applied to two exemplary compositions including 20 and 40 mol% PbSe. We envision that carefully tailored alternative protocols would either translate the entire polygons or expand their outer limits, thereby further widening the dispersion tunability. Such tailorability enables options for overcoming the limitation that for most IR applications there are far fewer total materials available for use, than those for visible systems (lower right corner) in **Figure 5e**.

### 3. Conclusion

The results presented here suggest that a simple multi-step thermal process can be utilized to induce GRIN profiles within manufacturable monolithic IR optical glasses. For the first time, we present a complete, mechanistic understanding of the compositionally specific morphology and microstructure that can be correlated to demonstrate resulting optical function in a broadband IR optical nanocomposite. This approach, suitable for optical glass-ceramics beyond the IR system illustrated here, can be used to realize novel broadband composites suitable for use in GRIN applications and in applications where tailored index or dispersion profiles are required. Demonstrated for a



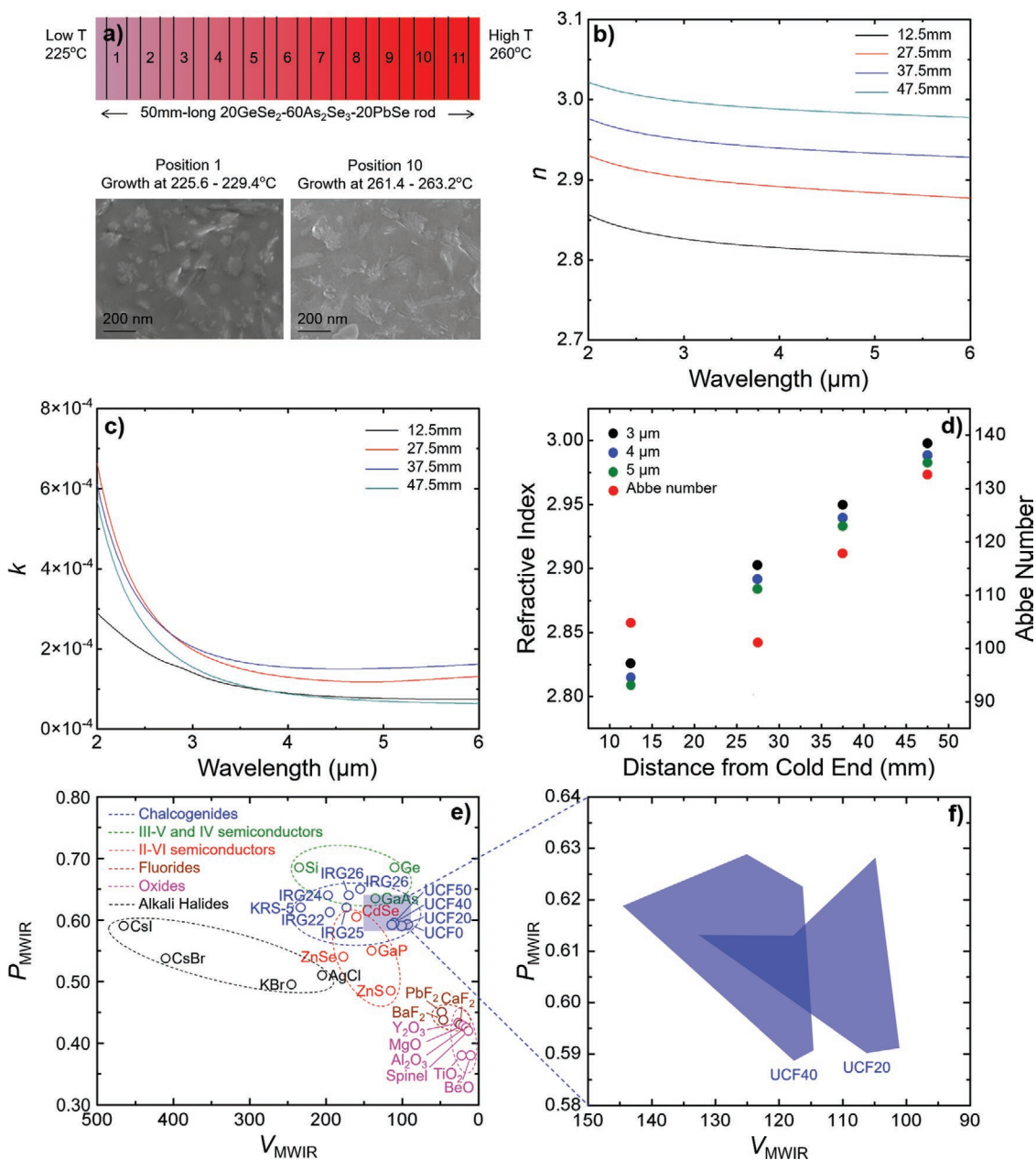


**Figure 5.** Evolution of GRIN. a) Gradient HT of a 50 mm long rod specimen with 20 mol% PbSe for 30 min at temperatures in a gradient furnace with a temperature of 225 °C near the cold end and 260 °C near the hot end. Corresponding BF TEM images taken from slice 1 cut from the cold end and the slice 10 taken from the hot end showing crystal phase in glass matrix. b) MWIR refractive index spectra of the slices 3, 6, 8, and 10 (distance from cold end shown in legend). c) MWIR optical loss spectra of the slices (distance from cold end shown in legend). d) Measured refractive indices at  $\lambda = 3, 4,$  and  $5 \mu\text{m}$  taken from (b) and corresponding Abbe numbers based on the three MWIR wavelengths. The error ( $< \text{approx. } 0.0005$ ) is within the size of the points shown. e) A refractive index dispersion map for various optical materials including chalcogenides, group III-V, group IV semiconductors, and group II-VI semiconductors, fluoride and oxide optical materials, and alkali halides. IRG22–IRG26 are commercially-available chalcogen-containing glasses from SCHOTT. KRS-5 is  $\text{TlBr}_{0.4}\text{I}_{0.6}$ . UCF0, UCF20, UCF40, and UCF50 correspond to pre-HT GAP-Se glasses with 0, 20, 40, and 50 mol% PbSe, respectively, fabricated at the University of Central Florida. f) The tailorability of MWIR dispersive properties for two different representative compositions of a GAP-Se system, enabled by current HT protocols.

finite composition space and utilizing knowledge of this composition-specific morphology, nucleation and growth behavior, crystalline phase formation, and optical property information, transparent and spatially varying broadband effective media for the IR have been realized. A gradient HT is used to induce

sub-wavelength, high index nanocrystalline phases within their amorphous matrix and spatially control their volume fraction, thereby realizing monolithic IR GRIN chalcogenide glass-ceramic nanocomposites. Our study highlights fundamental material behavior spanning the realm of glass-to-glass ceramic

science and how understanding of processing protocols at both macroscopic and microscopic levels correlate with morphological, structural, and compositional evolution enabling optical performance in a demonstrated single-component GRIN element. We demonstrate how a systematic approach to the quantitative design–processing–structure–property–performance engineering of these versatile tailorable glasses provides new opportunities for lens designers to extend design constraints and enable new optical functionalities not realizable through other homogeneous monolithic materials. This material science and engineering strategy demonstrates a new and completely unique paradigm to create unique IR optical composites with designed properties which will result in unique optical architectures for future systems with reduced SwaP. Along this work, further progress could be made to directly characterize the scattering behavior of IR electromagnetic waves travelling through the transmissive media. A direct measurement using angular detection of scattered light would reveal further insight into the impact of size, shape, volume fraction, and distribution of the particles on the resulting optical properties of nanocomposites, thereby strengthening an optimum pathway toward low-loss GRIN effective media.

#### 4. Experimental Section

**Glass Fabrication and Post HT:** Bulk chalcogenide glasses of  $(\text{GeSe}_2-3\text{As}_2\text{Se}_3)_{1-x}\text{PbSe}_x$  with varying PbSe concentrations (0 to 50 mol%) were prepared by a conventional melt-quenching technique. All glasses were prepared using high-purity raw materials (metals basis) from Alfa-Aesar: Se (99.999%), Ge (99.999%), Sb (99.999%), and Pb (99.999%). These elements were carefully weighed and batched in a nitrogen-purged MBraun Labmaster 130 glove box. The weighed batches (40 g) were loaded into cleaned fused quartz tubes and sealed under vacuum using a methane–oxygen torch to form sealed ampoules. Glass batches were melted in a rocking furnace overnight at a melting temperature of 850 °C. After rocking at elevated temperature, the furnace was cooled to a quench temperature of 650 °C, prior to removal from the furnace for quenching using compressed air flowing over the ampoule. To minimize the quench-related stress, glasses were annealed at 177 °C for 2 h and cooled to room temperature. The prepared glass rods were removed from the ampoules and cut into  $\approx 2$  mm thick slices using a slow speed saw. The glass slices or rods underwent either one-step or multi-step HT at various temperatures from 190 to 270 °C to convert them to glass-ceramics. For optical characterization, slices were polished using a polishing pad with 0.05  $\mu\text{m}$   $\text{Al}_2\text{O}_3$  slurry.

**Microstructure Analyses:** To determine the morphology and chemical composition of the glasses, cross-sectional TEM specimens were prepared by focused ion beam assisted milling followed by lift-out processing in a FEI Helios Nanolab 660 focused ion beam. The specimens were mounted on Cu grids and ion polished to  $\approx 50$  nm thickness for electron transparency. TEM imaging and SAED measurements of the cross-sectional specimens were carried out using a Talos F200X at 200 kV. XEDS data were collected using scanning transmission electron microscopy mode in the Talos F200X at 80 kV to assess any chemical segregation within the glass matrices.

**Optical Measurements:** Refractive indices of the bulk glasses were measured at wavelengths from 1.5 to 20  $\mu\text{m}$  and angles from 69° to 75°, using a J.A. Woollam IR-VASE spectroscopic ellipsometry system, including a Fourier transform infrared (FTIR) interferometer with a rotating compensator ellipsometer where IR light with an 8 mm beam spot is emitted by a Global. Signals were collected with a deuterated triglycine sulfate detector. The molecular structure of the glasses was investigated using a Bruker Senterra micro-Raman spectrometer. Raman scattering measurements were performed with an excitation laser

wavelength of 785 nm with 1 mW power. Data were collected using a 30 s exposure and was accumulated over five scans. Transmission spectra were recorded on samples using a Perkin Elmer Frontier (visible–NIR) and a Perkin Elmer Frontier Optica (NIR–LWIR) FTIR spectrometer. Measurements were averaged over 21 scans in the spectral range of 0.6 to 22  $\mu\text{m}$  with resolution of 8  $\text{cm}^{-1}$  at room temperature.

#### Supporting Information

Supporting Information is available from the Wiley Online Library or from the author.

#### Acknowledgements

This work was supported in part by the Defense Advanced Research Projects Agency under Air Force Research Laboratory contract FA8650-12-C-7225 through the M-GRIN Tech Area 2 program. The views, opinions, and/or findings expressed are those of the authors and should not be interpreted as representing the official views or policies of the Department of Defense or the U.S. Government (Distribution Statement "A": Approved for Public Release, Distribution Unlimited). The authors thank J. Gray, K. Wang, J. Maier, T. Clark, D. Hess, J. Banerjee, V. Bojan, H. Gong, L. Haney, D. Schulman, A. Swisher, and D. Werner at Pennsylvania State University for assisting in various aspects of microscopic material characterization and useful discussions. The authors also thank S. Misture at Alfred University for initial X-ray diffraction analysis on early candidate glasses as well as J. Veras at Lockheed Martin Corporation and C. Schwarz at the Ursinus College for useful discussions related to desirable optical performance criteria.

#### Conflict of Interest

The authors declare no conflict of interest.

#### Keywords

chalcogenide glass-ceramics, gradient refractive index, heat treatment, optical nanocomposites, spatially selective crystallization

Received: January 26, 2020

Revised: March 3, 2020

Published online:

- [1] X. H. Zhang, Y. Guimond, Y. Bellec, *J. Non-Cryst. Solids* **2003**, 326–327, 519.
- [2] D. H. Cha, H. Kim, Y. Hwang, J. C. Jeong, J. Kim, *Appl. Opt.* **2012**, 51, 5649.
- [3] H. Hisakuni, K. Tanaka, *Opt. Lett.* **1995**, 20, 958.
- [4] S. Ramachandran, J. C. Pepper, D. J. Brady, S. G. Bishop, *J. Lightwave Technol.* **1997**, 15, 1371.
- [5] G. Beadie, W. S. Rabinovich, J. Sanghera, I. Aggarwal, *Opt. Commun.* **1998**, 152, 215.
- [6] A. Saitoh, K. Tanaka, *Appl. Phys. Lett.* **2003**, 83, 1725.
- [7] E. A. Sanchez, M. Waldmann, C. B. Arnold, *Appl. Opt.* **2011**, 50, 1974.
- [8] Y. Kumaresan, A. Rammohan, P. K. Dwivedi, A. Sharma, *ACS Appl. Mater. Interfaces* **2013**, 5, 7094.
- [9] A. Saliminia, A. Villeneuve, T. V. Galstyan, S. LaRochelle, K. Richardson, *J. Lightwave Technol.* **1999**, 17, 837.

- [10] J. Hu, V. Tarasov, N. Carlie, N. Feng, L. Petit, A. Agarwal, K. Richardson, L. Kimerling, *Opt. Exp.* **2008**, *19*, 11798.
- [11] J. W. Choi, Z. Han, B. Sohn, G. F. R. Chen, C. Smith, L. C. Kimerling, K. A. Richardson, A. M. Agarwal, D. T. H. Tan, *Sci. Rep.* **2016**, *6*, 39234.
- [12] B. J. Eggleton, B. Luther-Davies, K. Richardson, *Nat. Photonics* **2011**, *5*, 141.
- [13] R. Frerichs, *J. Opt. Soc. Am.* **1953**, *43*, 1153.
- [14] S. Parvanov, V. Vassilev, K. Tomova, *Mater. Lett.* **2008**, *62*, 2021.
- [15] J. S. Sanghera, I. D. Aggarwal, *J. Non-Cryst. Solids* **1999**, *256-257*, 6.
- [16] X. H. Zhang, H. Ma, J. Lucas, *Opt. Mater.* **2004**, *25*, 85.
- [17] P. T. Lin, V. Singh, J. Wang, H. Lin, J. Hu, K. Richardson, J. D. Musgraves, I. Luzinov, J. Hensley, L. C. Kimerling, A. Agarwal, *Opt. Mater. Express* **2013**, *3*, 1474.
- [18] M. J. Booth, *Light: Sci. Appl.* **2014**, *3*, e165.
- [19] D. T. Moore, *Appl. Opt.* **1980**, *19*, 1035.
- [20] H. H. Li, *J. Phys. Chem. Ref. Data* **1980**, *9*, 561.
- [21] G. Zuccarello, D. Scribner, R. Sands, L. J. Buckley, *Adv. Mater.* **2002**, *14*, 1261.
- [22] R. A. Flynn, E. F. Fleet, G. Beadie, J. S. Shirk, *Opt. Express* **2013**, *21*, 4970.
- [23] D. Gibson, S. Bayya, V. Nguyen, J. Sanghera, M. Kotov, G. Drake, *Proc. SPIE* **2015**, *9451*, 94511P.
- [24] F. Bociort, *J. Opt. Soc. Am. A* **1996**, *13*, 1277.
- [25] P. K. Manhart, R. Blankenbecler, *Opt. Eng.* **1997**, *36*, 1607.
- [26] J. Teichman, J. Holzer, B. Balko, B. Fisher, L. Buckley. *Gradient Index Optics at DARPA*, The Institute for Defense Analyses, Alexandria, VA **2014**.
- [27] M. T. Flores-Arias, C. Bao, A. Castelo, M. V. Perez, C. Gomez-Reino, *Opt. Commun.* **2006**, *266*, 490.
- [28] K. Richardson, M. Kang, L. Sisken, A. Yadav, C. Blanco, M. Antia, S. Novak, B. Gleason, C. Smith, A. Buff, A. Lepicard, M. Dussauze, C. Schwarz, S. Kuebler, C. Grabill, C. Pantano, T. Mayer, A. Pogrebnyakov, C. Rivero-Baleine, A. Kirk, S. Mensah, M. Driggers, J. Hu, P. Lin, A. Agarwal, C. Li, W. Deng, *Proc. SPIE* **2018**, *10627*, 106270A.
- [29] S. N. Houde-Walter, D. T. Moore, *Appl. Opt.* **1985**, *24*, 4326.
- [30] S. Ji, M. Ponting, R. S. Lepkovicz, A. Rosenberg, R. Flynn, G. Beadie, E. Baer, *Opt. Express* **2012**, *20*, 26746.
- [31] G. Beadie, J. S. Shirk, A. Rosenberg, P. A. Lane, E. Fleet, A. R. Kamdar, Y. Jin, M. Ponting, T. Kazmierzak, Y. Yang, A. Hiltner, E. Baer, *Opt. Express* **2008**, *16*, 11847.
- [32] F. Qiu, T. Narusawa, J. Zheng, *Appl. Opt.* **2011**, *50*, 733.
- [33] L. Sisken, *Ph.D. Thesis*, University of Central Florida, Orlando, FL **2017**.
- [34] L. Sisken, C. Smith, A. Buff, M. Kang, K. Chamma, P. Wachtel, J. D. Musgraves, C. Rivero-Baleine, A. Kirk, M. Kalinowski, M. Melvin, T. S. Mayer, K. Richardson, *Opt. Mater. Express* **2017**, *7*, 3077.
- [35] M. Kang, L. Sisken, J. Cook, C. Blanco, M. Richardson, I. Mingareev, K. Richardson, *Opt. Mater. Express* **2018**, *8*, 2722.
- [36] M. Kang, A. M. Swisher, A. V. Pogrebnyanov, L. Liu, A. Kirk, S. Aiken, L. Sisken, C. Lonergan, J. Cook, T. Malendevych, F. Kompan, I. Divliansky, L. B. Glebov, M. C. Richardson, C. Rivero-Baleine, C. G. Pantano, T. S. Mayer, K. Richardson, *Adv. Mater.* **2018**, *30*, 1803628.
- [37] A. Buff, *Master Thesis*, University of Central Florida, Orlando, FL **2016**.
- [38] A. Yadav, M. Kang, C. Smith, J. Lonergan, A. Buff, L. Sisken, K. Chamma, C. Blanco, J. Caraccio, T. Mayer, C. Rivero-Baleine, K. Richardson, *Phys. Chem. Glasses* **2017**, *58*, 115.
- [39] C. Goncalves, M. Kang, B.-U. Sohn, G. Yin, J. Hu, D. T. H. Tan, K. Richardson, *Appl. Sci.* **2018**, *8*, 2082.
- [40] G. Yang, X. Zhang, J. Ren, Y. Yunxia, G. Chen, H. Ma, J. L. Adam, *J. Am. Ceram. Soc.* **2007**, *90*, 1500.
- [41] H. Wang, X. Zhang, G. Yang, Y. Xu, H. Ma, J. L. Adam, Z. Gu, G. Chen, *Ceram. Int.* **2009**, *35*, 83.
- [42] L. Sisken, M. Kang, J. M. Veras, C. Lonergan, A. Buff, A. Yadav, D. McClane, C. Blanco, C. Rivero-Baleine, T. S. Mayer, K. Richardson, *Adv. Funct. Mater.* **2019**, *29*, 1902217.
- [43] K. Richardson, A. Buff, C. Smith, L. Sisken, J. Musgraves, P. Wachtel, T. Mayer, A. Swisher, A. Pogrebnyakov, M. Kang, C. Pantano, D. Werner, A. Kirk, S. Aiken, C. Rivero-Baleine, *Proc. SPIE* **2016**, *9822*, 982205.
- [44] A. Yadav, A. Buff, M. Kang, L. Sisken, C. Smith, J. Lonergan, C. Blanco, M. Antia, M. Driggers, A. Kirk, C. Rivero-Baleine, T. Mayer, A. Swisher, A. Pogrebnyakov, A. Hilton Jr., G. Whaley, T. Loretz, A. Yee, G. Schmidt, D. Moore, K. Richardson, *Int. J. Appl. Glass Sci.* **2019**, *10*, 27.
- [45] D. A. Porter, K. E. Easterling, M. Sherif, *Phase Transformations in Metal and Alloys*, CRC Press, Boca Raton, FL **2009**.
- [46] J. Chen, W. Z. Shen, *J. Appl. Phys.* **2006**, *99*, 013513.
- [47] R. Zallen, M. L. Slade, A. T. Ward, *Phys. Rev. B* **1971**, *3*, 4257.
- [48] U. Kreibig, M. Vollmer, *Optical Properties of Metal Clusters*, Springer, Berlin **1995**.
- [49] N. Carlie, presented at SPIE Photonics West 2013, San Francisco, CA, February **2013**.